## 2000 Turbomachinery Committee and Structures & Dynamics Committee Best Paper Award

A. F. Storace

D. C. Wisler

H.-W. Shin

B. F. Beacher

GE Aircraft Engines
Cincinnati, OH 45215

F. F. Ehrich

Z. S. Spakovszky

M. Martinez-Sanchez

Massachusetts Institute of Technology,
Cambridge, MA

S. J. Song
Seoul National University,
Seoul, Korea

# Unsteady Flow and Whirl-Inducing Forces in Axial-Flow Compressors: Part I—Experiment

*An experimental and theoretical investigation has been conducted to evaluate the effects seen in axial-flow compressors when the centerline of the rotor is displaced from the centerline of the static structure of the engine. This creates circumferentially nonuniform rotor-tip clearances, unsteady flow, and potentially increased clearances if the rotating and stationary parts come in contact. The result not only adversely affects compressor stall margin, pressure rise capability, and efficiency, but also generates an unsteady, destabilizing, aerodynamic force, called the Thomas/Alford force, which contributes significantly to rotor whirl instabilities in turbomachinery. Determining both the direction and magnitude of this force in compressors, relative to those in turbines, is especially important for the design of mechanically stable turbomachinery components. Part I of this two-part paper addresses these issues experimentally and Part II presents analyses from relevant computational models. Our results clearly show that the Thomas/Alford force can promote significant backward rotor whirl over much of the operating range of modern compressors, although some regions of zero and forward whirl were found near the design point. This is the first time that definitive measurements, coupled with compelling analyses, have been reported in the literature to resolve the long-standing disparity in findings concerning the direction and magnitude of whirl-inducing forces important in the design of modern axial-flow compressors.* [DOI: 10.1115/1.1378299]

## 1.0 Introduction and the Nature of the Issues

**1.1 Introduction.** Increases in clearances resulting from rubs between rotating and stationary turbomachinery components operating at tight levels of clearance most frequently result from forces induced by the following situations: rotor unbalance (associated with imperfections in rotor manufacture or assembly), lateral deceleration during a hard landing, lateral forces induced by high-g and high-rate-of turn maneuvers, thermal bowing and/or asymmetric ovalization of the casing, especially for fans.

However, a potentially much more destructive mechanism for inducing rubs is whirl instability. Any radial deflection of the rotor relative to the stator creates circumferentially nonuniform clearances and unsteady aerodynamic forces on the rotor as each blade traverses the varying clearance gap. These unsteady forces are orthogonal to the deflection and therefore are a significant driver of rotor whirl instabilities. The forces increase in magnitude as the deflection increases so that above the onset speed, where destabilizing forces overwhelm the stabilizing damping forces, the deflections are ultimately limited only by damage to the interacting parts or by damping forces. Consequently an accurate determination of their magnitude and direction is of major importance in the design of safe, stable turbomachinery components. Examples of whirl are hysteretic whirl, whirl associated with fluids trapped within cylindrical rotor cavities and plain journal bearings, etc.

**1.2 The Nature of the Issues.** The unsteady, destabilizing, aerodynamic cross-axis stiffness force that promotes rotor whirl was first postulated by Thomas [1] and Alford [2] to explain rotor

whirl instabilities seen in steam turbines and jet engines respectively. Therefore, this force is generally referred to as the Thomas/Alford force.

*Whirl in Turbines.* For a deflected turbine rotor, it has been shown experimentally that the airfoils in the closure zone are more highly loaded by aerodynamic forces than the airfoils in the open clearance zone because the former are operating more efficiently [3]. This situation is shown schematically in Fig. 1(*a*) for a turbine rotor whose centerline has been displaced upward along the ordinate by an amount $+Y$. This gives minimum clearance at the top of the turbine and maximum clearance at the bottom. The forces at these two locations are the vector sum of the mean blade force, $F_m$, and the unsteady blade force resulting from the centerline offset, $F_u$. As suggested by Thomas [1], summing the forces *perpendicular* to the axis of displacement results in a net force, $F_X = F_m + F_u$, due to the difference in airfoil loading. Since $F_X$ acts normal to the axis of displacement, it is called a cross-axis (cross-coupled) stiffness force. As seen in Fig. 1(a), the direction of $F_X$ acts to drive the rotor in orbital (whirling) motion about the nondisplaced centerline in the same direction as rotor rotation, i.e., $F_X$ promotes forward whirl for turbines. Thomas postulated the following model to compute a cross-coupled aerodynamic stiffness coefficient in terms of the acting torque and a $\beta$ coefficient:

$$K_{XY} = \frac{F_X}{+Y} = \frac{T\beta}{D_P H} \qquad (1)$$

Measurements of transverse destabilizing forces in unshrouded turbines give positive $\beta$ values in the range from 2 to 5 [4–7].

*Whirl in Compressors.* Alford [2] hypothesized the same phenomenon for compressors, whereby aerodynamic, cross-axis forces caused by asymmetric tip clearance feed energy into the whirling motion of the rotor. Alford reasoned that during rotor whirl, the circumferential variation in radial tip clearance causes a
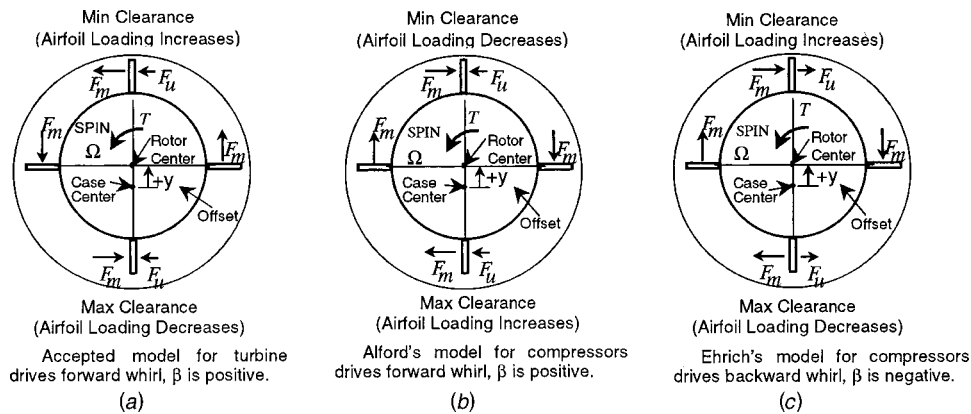
**Fig. 1 Models of whirl-inducing forces in turbines and compressors. Net force $F_x = F_m + F_u$ acts perpendicular to the axis of displacement and drives rotor whirl; see Appendix B1.**

circumferential variation in efficiency so that the blading with the smallest clearance would be the most efficient. Alford further hypothesized that the compressor would pump to a circumferentially uniform exit static pressure and therefore the more efficient blading at tight clearance would have a lower loading than the blading with larger clearance 180 deg away. This situation, illustrated in Fig. 1(b), shows that the net force, $F_X$, tends to cause forward rotor whirl. Thus, Alford concluded that compressors have positive $\beta$'s so that whirl-inducing forces for both compressors and turbines are in the same direction.

Ehrich [8] hypothesized differently from Alford. He reasoned that compressor airfoils with the smaller clearance would sustain a higher static pressure differential across their tips and would therefore be more highly loaded than the airfoils with larger clearance, 180 deg away. As shown in Fig. 1(c), this dictates that the net destabilizing force in compressors, $F_x$, tends to produce rotor whirl counter to the direction of rotation. Thus Ehrich concluded that compressors tend to have negative $\beta$ coefficients so that the direction of whirl-inducing forces for compressors would be opposite to those for turbines.

There has been a disparity in the findings in the literature concerning the direction of rotor whirl in compressors. Vance and Laudadio [9] found experimentally that the Thomas/Alford force is rotor-speed dependent and mostly positive, except for some special combinations of rotor speed and stage torque where the direction of the force was reversed. Colding-Jorgensen [10] found the same generality for the shape and slope of the relationship of $\beta$ coefficient versus flow coefficient as later reported by Ehrich [8], but the Colding-Jorgensen results suggested a more positive level of the parameter than the negative levels reported in Ehrich's work. Ehrich [8] further showed that the experimental data of Vance and Laudadio [9] implied that, for certain values of torque and speed in their low-speed blower tests, the destabilizing forces tend to drive backward whirl. Other evidence was also accumulating in theoretical and experimental results of Yan et al. [11] to indicate negative $\beta$ coefficients for compressors.

In engine field experience, aerodynamic cross-axis forces were cited by Akin et al. [12] as the destabilizing mechanism in the high-pressure rotor instability of the TF30 P111 + engine when it went into production in mid-1986. Vibration reject rates were as high as 50 percent until the instability was eliminated by using a squeeze-film damper at the high pressure turbine bearing.

In view of the importance of the $\beta$ coefficient in designing stable turbomachinery components, the disparity between Alford's and Ehrich's conjectures, the mixed findings of researchers on the issues, the need for designers to often use very conservative methods, and the absence of a decisive resolution of rotor whirl issues, we formulated the experimental and analytic program described in Parts I and II.

## 2.0 Objectives and Definitions

**2.1 Objectives.** The overall goal of Part I was to provide a definitive resolution of the long-standing disparity in findings concerning the direction and magnitude of rotor whirl in compressors.

There were three major objectives of Part 1. The first was to quantify any changes in compressor performance and airfoil loading produced in compressors when the rotor centerline becomes displaced or offset from that of the stator. The second was to determine which of the two models best describes whirl in compressors, the Alford Model of Fig. 1(b) or the Ehrich model of Fig. 1(c). The third was to determine the direction and magnitude of rotor whirl-inducing, aerodynamic forces in axial-flow compression systems used in modern turbomachinery, including their design implications.

Comparing the results from analytical and computational models relative to the experimental data will be the subject of Part II.

**2.2 Definitions.** The following definitions will be helpful.

*Rotor whirl instability*: Unstable rotor whirl is defined as the self-excited orbital motion of the rotor centerline about its nominal or undisplaced centerline induced by a destabilizing tangential force, which overcomes the stabilizing external damping forces. There are several potential sources of such destabilizing forces. This paper focuses on the Thomas/Alford forces.

*Beta coefficient*: the "Thomas/Alford Parameter," originally conceived as the change in thermodynamic efficiency per unit change in blade tip clearance, expressed as a fraction of blade height. In practice $\beta$, as defined by Eq. (1), is a normalized value of the cross-coupled stiffness.

*Forward whirl*: whirl whose direction is the same as that of the engine rotor rotation or spin. The $\beta$ coefficient is positive for forward whirl.

*Backward whirl*: whirl whose direction is opposite to that of the engine rotor rotation or spin. The $\beta$ coefficient is negative for backward whirl.

*Aerodynamic cross-axis force*: the net unbalanced aerodynamic force that acts perpendicular to rotor radial deflection to drive rotor whirl.

## 3.0 Experimental Test Program

We set up a test program in the GE Low Speed Research Compressor to simulate the eccentricity of a whirling rotor and measure the nonuniform, unsteady flowfield that develops.

**3.1 Low Speed Research Compressor (LSRC).** The LSRC is an experimental facility that duplicates the relevant aerodynamic features of axial flow compressors in modern gas turbine engines in a large, low-speed machine where very detailed investigations of the flow can be made. Aerodynamic similarity for

Mach number and Reynolds number is used in scaling the high-speed airfoils to their low-speed counterparts. This method of testing has proven reliable for over forty years in understanding and designing HP compression systems provided the phenomena being studied are Reynolds number dependent and not compressibility dependent.

The LSRC, which has a constant casing diameter of 1.524 m (60.0 in.), was set up with four identical stages in order to simulate the repeating stage environment. The third stage was the test stage. The blading was representative of current design practice.

Three different low-speed blading configurations were tested. The first two, called Compressors $A$ and $B$ respectively, are typical of modern designs and have high hub/tip ratios of 0.85 with low-aspect-ratio, high-solidity blading and shrouded stators. These two compressors are low-speed, aerodynamic models of the middle and rear block of highly loaded, high-reaction (65–70 percent) HP compressors in commercial gas turbine engines currently in service. Compressor $C$, also in commercial engine service, has cantilevered stators and blading with a lower hub/tip ratio of 0.70, lower reaction of 0.55, and higher aspect ratios than the others have. Additional information about the LSRC testing technique and the blading is available in [13–15]. Blading details for all three compressors are given in Table 2 of Appendix A.

A cross section showing the test stage for Compressor $A$ is given in Fig. 2. The stators are shrouded so that there is no clearance between the end of the stator airfoil and the hub under the airfoil. The seal tooth inhibits flow leakage from the trailing edge region through the seal cavity upstream to the leading edge region. Consequently, the leakage flowfield across the rotor tip is very different from that in the stator hub.

Only Compressor $A$ was tested with the stator centerline offset from that of the rotor, as described below. All three compressors were tested at different axisymmetric clearances without offset to obtain the required input for the models in Part II.

**3.2 Offset and Clearance Conditions.** The use of large, precision offset rings and offset bearing supports enabled us to assemble the LSRC with the centerline of the stator casing offset (displaced) relative to the centerline of the rotor and its drive mechanism. The offset is shown schematically in Fig. 3. This process of moving the entire stator assembly relative to the rotor to achieve the offset significantly reduced both the cost and complexity of the test program as compared to moving the complex and massive rotor drive mechanisms.

Tests were performed for Configuration A with two displacements of the casing centerline: a larger displacement of 0.1905 cm (0.075 in) and a smaller one of 0.0965 cm (0.038 in). The larger
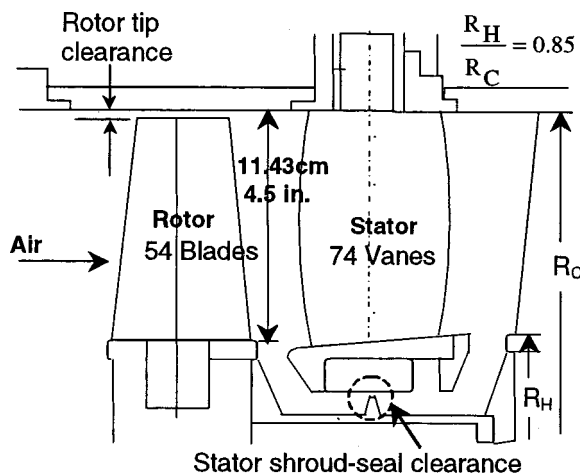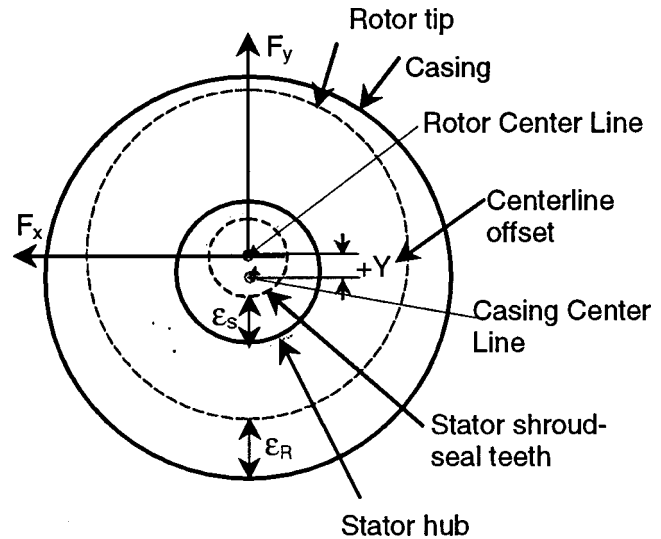


**Fig. 3 LSRC configuration for centerline offset tests showing circumferential variation in rotor tip clearance $\varepsilon_R$, and stator shroud seal clearance, $\varepsilon_s$. Looking down on spinning, non-whirling eccentric rotor with casings moved relative to rotor assembly; see Appendix B2.**

displacement exceeded the baseline rotor tip clearance by 0.0279 cm (0.011 in.). Therefore, to avoid both significant damage to the LSRC test hardware from a rub and the resulting safety issues, we ground the rotor tip and the stator shroud seal to allow both to run at the absolute minimum safe clearance judged to be 0.051 cm (0.020 in.). This permitted the vehicle to enter rotating stall. Although this process increased the magnitude of the average clearances, the levels of centerline offset and clearance magnitudes bounded those of practical field experience where clearances increase in high-time engines.

The offsets gave the corresponding values of minimum and maximum clearance for the rotor-tip and the stator shroud seal-tooth as shown in Table 3 of Appendix A. Precision run-outs gave clearance variations from nominal around the circumference of $\pm0.0152$ cm (0.006 in.). The offset was measured to be accurate to within $\pm0.0102$ cm (0.004 in.).

While the rotor did not actually whirl in these tests, the static shaft offset was intended to approximate the flowfield present in whirling rotor motion to allow evaluation of the dominant aerodynamic forces contributing to rotor whirl. The effects of the additional forces in an actual whirling rotor are analyzed in Part II.

**3.3 Instrumentation**

*Steady-state Instrumentation.* High-resolution pressure transducers, accurate to $\pm0.010$ percent of the full-scale values of either 0.068 or 0.136 bar (1 or 2 psi), were used to record steady-state static and total pressures for determining both overall compressor performance and the static pressures on the stator airfoil surfaces. Frequent calibrations were conducted. A strain-gage torque meter, accurate to $\pm0.07$ percent of measured torque, was used to deduce shaft work input to quantify compressor efficiency. Overall measurement accuracy is as follows: Flow coefficient and pressure coefficient are accurate to within $\pm0.15$ percent and efficiency to within $\pm0.25$ points.

*Dynamic Instrumentation.* A total of 64 ultra-miniature, high-response Kulite model LQ-125 pressure transducers, having a frequency response of 20 kHz, were imbedded inside the rotor airfoil surfaces to measure the unsteady static pressures acting on the suction and pressure surfaces. The locations of the Kulites, shown in Table 4 of Appendix A, were selected to provide resolution of both chordwise and spanwise gradients. Small pressure ports pneumatically connected the sensor to the measurement surface.



**Fig. 2 Schematic showing cross section of compressor A blading**

The port diameters were sized properly at 0.08128 cm (0.032 in.) and the lengths were small enough at 0.0406 cm (0.016 in.), as defined by Doebelin [16], so as not to attenuate the periodic unsteady pressures.

The transducers were calibrated after installation in the airfoils by using both a pressurized/evacuated chamber and a dynamic frequency-response calibrator. The transducer accuracy was ±1.0 percent. The response was unattenuated with no phase shifting up to 1400 Hz (the limit of the calibrator used) or two times blade passing frequency.

*Data Sampling and Signal Processing.* The signals from the pressure transducers were digitized and ensemble-averaged. A Kinetic System analog-to-digital converter was used to digitize the data signals using phase locked sampling at constant time increments. The analog data were low-pass filtered at 1 kHz to avoid aliasing. The use of 200 ensemble averages greatly reduced the effects of time-unresolved unsteadiness. A once-per-revolution pulse from an optical encoder in the casing sensed the trigger airfoil on the rotor blade and initiated the sampling for the data windows for each rotor revolution.

### 3.4 Data Reduction

*Calculation of Unsteady Pressures.* Since the pressure transducers were mounted in seven different airfoils on the 54-bladed rotor disk, great care was taken in time-shifting and synthesizing these data onto one representative airfoil to construct the unsteady pressure variation experienced by the rotor airfoils during a rotor revolution. The raw pressure data for each transducer were processed using fast Fourier transform (FFT) methodology to give a filtered waveform consisting only of the first harmonic. An example of the raw data is presented in Fig. 4(*a*) and the results from its FFT analysis to obtain the Fourier coefficients are shown in Fig. 4(*b*). The first harmonic is dominant. The 54th and 74th harmonics in the figure are associated with 54 rotors and 74 stators. An example of the circumferential variation of unsteady pressure determined from the first harmonic is shown in Fig. 4(*c*).

The unsteady pressures measured at the discrete locations on the airfoil surfaces were bidirectionally curve-fit along the radial and chordwise directions to obtain continuous pressure distributions on the suction and pressure surfaces. Our confidence levels in being able to integrate the unsteady blade pressures for the given Kulite coverage was about 95 percent. This was assessed by randomly removing data from several kulites from the analysis, re-processing the data, and comparing the forces obtained from the pressure integration. DC-level comparisons were not made because the Kulite transducers were not installed in the centered-rotor configuration.

*Calculation of the Thomas/Alford Force.* By using the unsteady pressure distributions computed above and the geometric orientation of the airfoil surfaces in the compressor, we integrated over the airfoil surfaces to obtain the unsteady forces acting on the various airfoils around the circumference. We resolved the unsteady forces into their tangential and radial components using the local blade coordinate system shown in Fig. 5; see Appendix B3a.

Next we computed the component of force acting perpendicular to the direction of rotor offset, $F_x$ (the Thomas/Alford force). To do this, we transformed the tangential and radial blade forces in the local blade coordinate system of Fig. 5 to the global coordinate system fixed to the bladed disk, also shown in Fig. 5. We then algebraically summed the individual forces to get the net cross-axis stiffness force $F_x$, and the net direct positive stiffness force $F_Y$; see Appendix B3b.

*Calculation of the Beta Coefficient.* The Beta coefficient is calculated from Eq. (1) using the torque and the slope (cross-axis stiffness, $K_{XY}$) of the Thomas/Alford force $F_X$ plotted versus rotor offset.



Raw waveform of measured pressure

(*a*)



Fast Fourier Transform of raw waveform

(*b*)



Circumferential variation of unsteady pressure using first Fourier Coefficient.
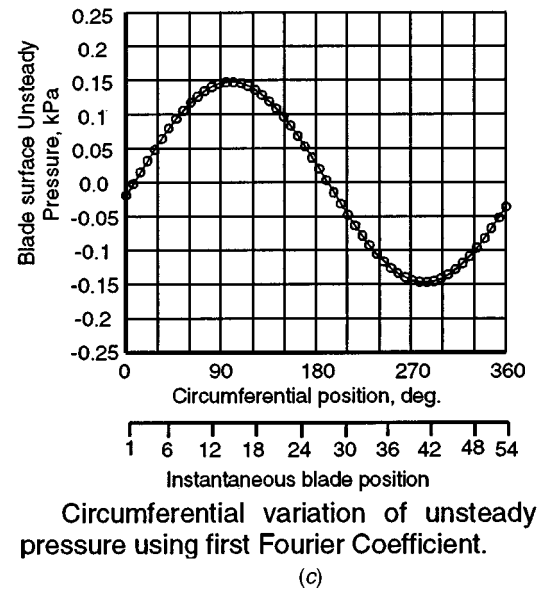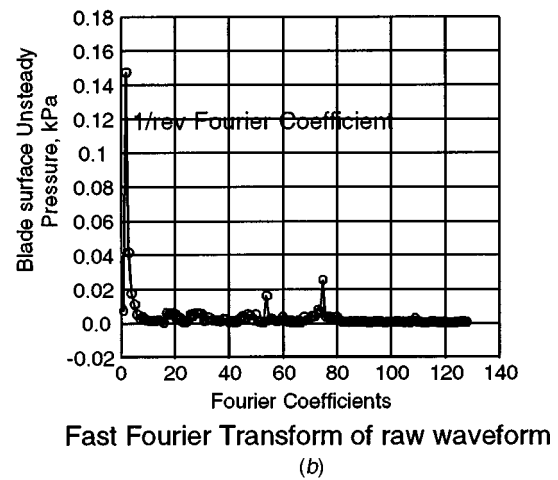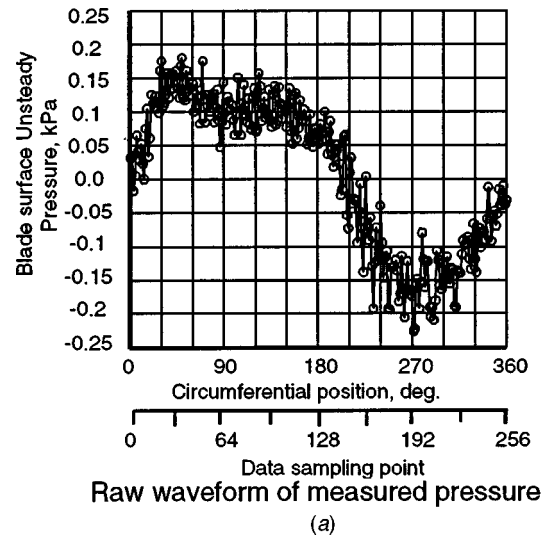
(*c*)

**Fig. 4 Typical example showing the circumferential variation in unsteady static pressure obtained from a Kulite pressure transducer embedded in a rotor airfoil (96 percent span and 50 percent chord for the large rotor offset): (*a*) raw data, (*b*) FFT of raw data, (*c*) filtered signal.**
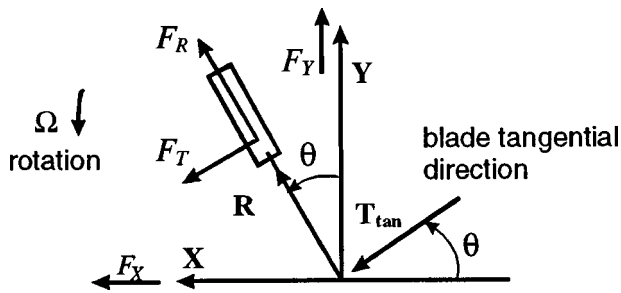
**Fig. 5 The two coordinate systems used to resolve blade forces: (1) blade fixed coordinate ($T_{tan}$,$R$), (blade geometry defined in this system); (2) rotating coordinate ($X$, $Y$) (the blade azimuth angle $\theta$ is defined in this coordinate system); see Appendix B3**

## 4.0 Effects of Clearance Variation and Centerline Offset on Overall Compressor Performance

Compressor performance is presented in this section as a four-stage average of pressure coefficient and efficiency plotted as a function of flow coefficient. The curve of pressure coefficient versus flow coefficient is called the pressure characteristic. Stall margin is computed for these low-speed tests in terms of throttle margin, TM, as defined in the nomenclature.

Variations in loading levels from high flow (low-loading) to stall were achieved by varying mass flow rate through the compressor using a discharge throttle. Lines of constant throttle setting are shown in the figures to indicate the different loading levels along the pressure characteristic. The tests were run at the design tip speed of 64.0 m/s (210 ft/sec), which required a rotational speed of approximately 804 rpm. This gave a Reynolds number of $3.6 \times 10^5$, which is sufficiently above the knee in the Reynolds number-loss curve to be representative of engine conditions.

**4.1 Baseline Performance.** The baseline performance of Compressor A, shown as Curves A1 in Figs. 6 and 7, was established with no centerline offset and with circumferentially uniform, nominal levels of rotor-tip clearance and stator shroud-seal clearance given in Table 3 of Appendix A. The design point is shown in both figures. The negative slope of the baseline pressure characteristic over all of the flow range from high flow to near peak pressure provides stable operation over this range, after which it begins to roll over. Stall occurs at a flow coefficient of about 0.335, as indicated by the short vertical line at the low-flow end of the pressure characteristic. Baseline Compressor A has high efficiency that peaks at 90.4 percent. It also has a good throttle margin of 30.2 percent, as indicated by the 17.9 percent flow range from the design point to stall. This baseline is the performance standard against which all of the other configurations will be compared.

**4.2 Effect of Axi-symmetric Clearance Variation on Performance.** The effects of varying axisymmetric (circumferentially uniform) clearance on the performance of Compressor A are shown relative to the baseline performance in Fig. 6. The clearance variation was obtained without centerline offset and thus is typical of what occurs in a uniform rotor tip rub. Both rotor tip clearance and stator shroud-seal clearance were varied independently so that we could separate the effects. Detailed surveys of flow properties (not included in this paper) showed that when rotor tip clearance alone was increased, the dominant effect was seen in the outer 25 percent of span. Similarly when the stator seal clearance alone was increased, the dominant effect was seen in the inner 25 percent of span.

Looking first at Curves A2 in Fig. 6 showing the effects of doubling only the stator shroud-seal clearance, we see that peak pressure rise and efficiency are reduced by 3.4 percent and 0.90
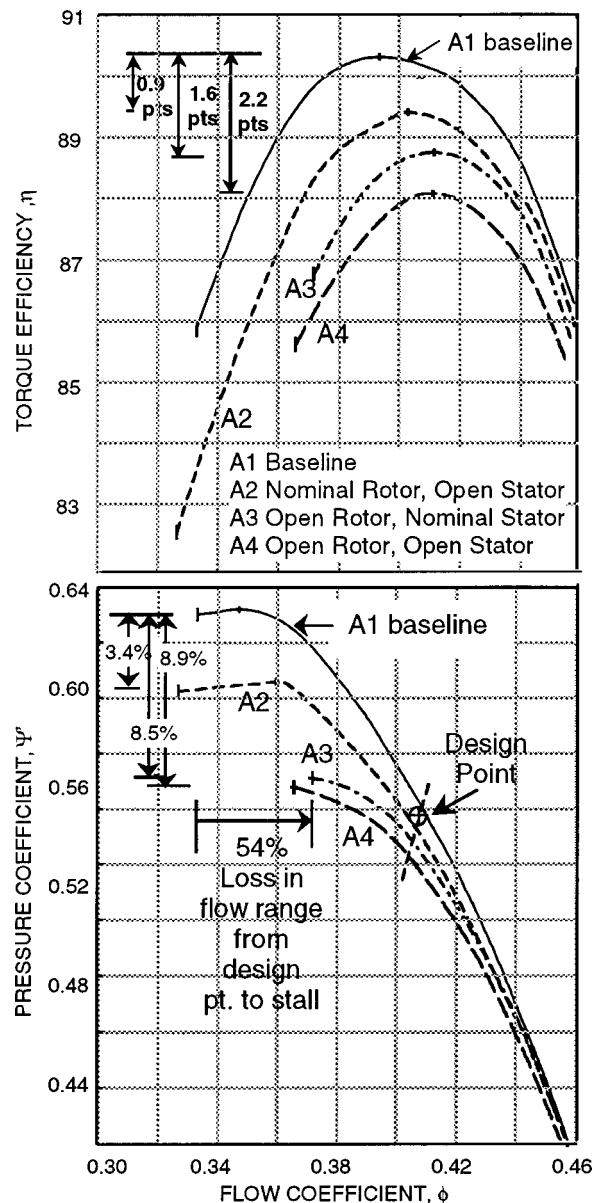


**Fig. 6 Overall performance of compressor A showing the effects of variation in axisymmetric clearances relative to baseline performance. Compressors A1–A4 are defined in Table 3 of Appendix A. Data accuracy is identical to that for Fig. 7, therefore data symbols are removed for clarity.**

points, respectively. However, stalling flow is nearly unaffected because this is tip-sensitive blading with respect to stall onset; thus reasonable changes in hub clearances will not significantly affect the flow level at which stall onset occurs.

Looking next at Curves A3 in Fig. 6, which show the effects of doubling only the rotor tip clearance, we see that all performance quantities are affected significantly. There is a 8.5 percent reduction in peak pressure rise, a 1.6 point loss in efficiency, a 54 percent loss in flow range between the design point and stall, and a throttle margin of 11.1 percent, which is 37 percent of the baseline value. Being a tip-sensitive compressor, changes in rotor tip clearance significantly affect stall onset.

Opening both rotor tip clearance and stator shroud-seal clearance produces the expected results of further loss in pressure rise and efficiency but little further change in stalling flow range, as shown by Curves A4 in Fig. 6.
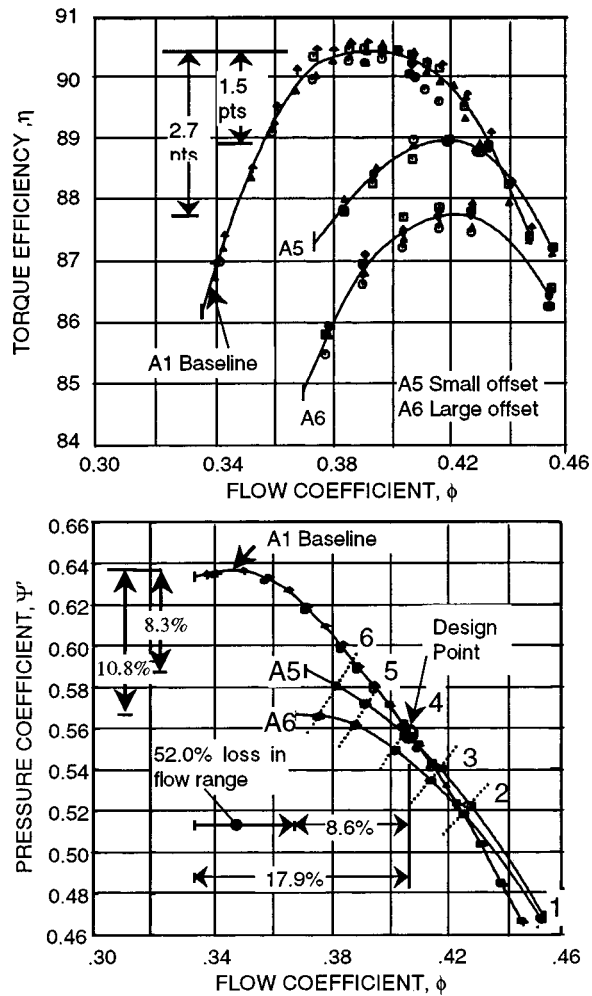
**Fig. 7 Overall performance of Compressor A for rotor center-line offset tests relative to baseline performance**

$$\Delta \overline{\varepsilon}_{r,s} = \left( \frac{\overline{\varepsilon}_r - \overline{\varepsilon}_{r,\mathrm{Baseline}}}{H} + \frac{\overline{\varepsilon}_s - \overline{\varepsilon}_{s,\mathrm{Baseline}}}{H} \right) \times 100 \text{ percent}$$

Note that all clearances are normalized by the blading span of 11.43 cm (4.50 in.). This approach of adding clearances was taken to evaluate the degree of linearity in the performance derivatives. We evaluated derivatives in terms of average clearances since changes in pressure coefficients, efficiency, and loading, which are of primary interest for assessment of Thomas/Alford forces, typically vary systematically with changes in average clearance. Loss in stall margin typically correlates with changes in maximum clearance, but that is of less interest here.

The performance derivatives for axisymmetric Compressors A1–A4 were computed at the peak efficiency and increased loading points in Fig. 6. The results, shown in Fig. 8 as open symbols, describe a linear sensitivity to change in total average clearance within 0.150 variance for the pressure derivative and 0.008 for the efficiency derivative.

The performance derivatives were also computed for both the small and large offset result described previously in Fig. 7. These derivatives, shown as the solid symbols in Fig. 8, have nearly the same linear sensitivity as those for the axisymmetric tests. This provides high confidence that parallel compressor theory and the methodology of Part II are appropriate.
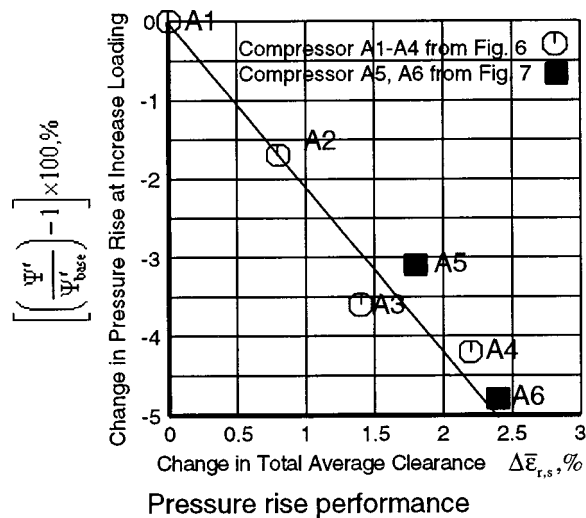
**4.5 Performance of Compressors B and C.** The pressure and efficiency characteristics for Compressors B and C are presented in Fig. 9. The configurations, labeled Curves B1, B2, B3, C1, and C2, are identified in Table 3 in Appendix A. These results will be used in Part II in Ehrich's methodology for whirl analysis.

## 5.0 Effects of Centerline Offset on Airfoil Loading for Compressor A
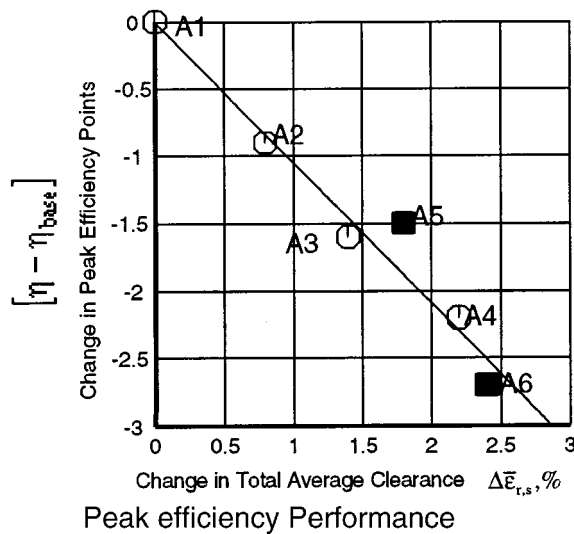
**5.1 Unsteady Loading on Rotor Airfoils.** Unsteady pressures on the rotor airfoils were measured as the rotor traveled through varying levels of clearances caused by the centerline offset. Suction surface pressures were subtracted from pressure surface pressures to give unsteady pressure difference (loading) on the airfoil. Representative results showing this loading for three clearance levels around the circumference are presented in Fig. 10 as contours of differences in unsteady static pressure. The color red indicates the highest loading and blue indicates the lowest loading. Figure 10(a, b, c) show the rotor at near minimum clearance, nominal clearance, and near maximum clearance respectively. The measured, steady-state, surface static pressure distribution at 80 percent span for the rotor airfoil is shown in Fig. 10(d).

It is clear that airfoil unsteady loading across the span increases in the region of minimum clearance (red contours in Fig. 10a) and decreases in the region of maximum clearance (blue contours in Fig. 10(c)) relative to the mean loading at nominal clearance in Fig. 10(b). It is also clear from Fig. 10 that, near the rotor tip in Zone A, the airfoil loading increases at near minimum clearance and decreases at near maximum clearance. This finding confirms the correctness of Ehrich's hypothesis in Fig. 1(c) about the nature of rotor whirl-inducing forces in compressors as discussed in Section 1.2.

In trying to explain the driving mechanisms for rotor whirl in turbomachinery, previous investigators have concentrated only on the effects of variation in rotor tip clearance. Our unsteady data in Fig. 10 show an additional feature needing attention in whirl analyses, namely, the effect of clearances in the hub region as an additional driver of rotor whirl. The changes in stator shroud-seal clearance and any radial redistribution of flow produce a change in hub loading on the rotor in Zone B. As seen in Figs. 10(a, c), the unsteady forces in the hub increase (red contour) at tight clearance and decrease (blue contour) at more open clearance. While it is known that varying stator hub/shroud clearance affects both compressor aerodynamic performance and local hub airfoil/drum

**4.3 Effect of Centerline Offset Having Increased Average Clearances on Performance.** The pressure and efficiency characteristics for the two levels of casing centerline offset are compared in Fig. 7 to those for the baseline configuration. As expected, the offset configurations with their larger average and maximum clearances, shown as Curves A5 and A6, have lower efficiencies and lower peak pressure rise than those for the baseline Curves A1. There is an 8.3 percent, and 10.8 percent loss in peak pressure and 1.5 point and 2.7 point loss in peak efficiency, respectively, for the small and large offsets. Throttle margin is 11.7 percent, which is 39 percent of the baseline value. Thus, stall margin has suffered considerably. Note that there is little change in loss of stalling flow range between small and large offsets.

**4.4 Applicability of Parallel Compressor Theory.** Two of the models used to compute $\beta$ coefficients in Part II of this paper rely on the validity of parallel compressor methodology. In addition, Part II will analyze our data by separating it into that for the outer 50 percent span (influenced by rotor tip clearance) and that for the inner 50 percent span (influenced by stator seal clearance), followed by a synthesis of these results. In order to gain confidence in these approaches, we evaluated the Compressor A performance derivatives for the offset tests relative to those for the axisymmetric tests.

Both the change in pressure rise and the change in efficiency were determined for the corresponding change in total average clearance from the baseline clearances as expressed by the following equation:
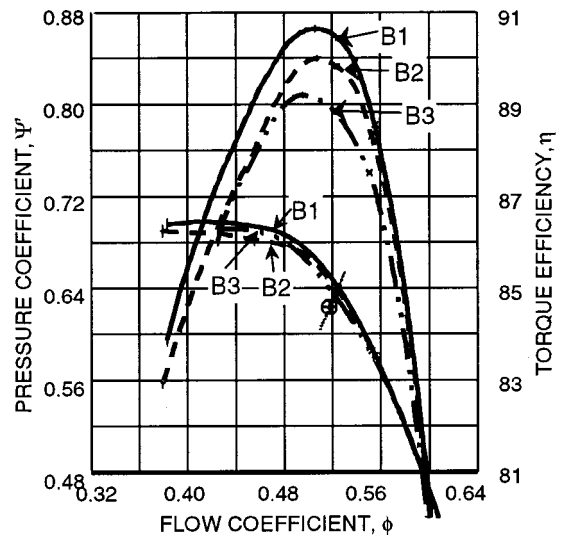
**Fig. 8 Performance derivatives for compressor A in terms of change in total average clearance from baseline clearance levels**



**Fig. 9 Performance characteristic for compressors *B* and *C***

loading [13,17], until now this effect has not been incorporated into documented rotor-whirl analyses. In that sense, incorporating these findings into the analyses presented in Part II constitutes a new approach to whirl analysis.

**5.2 Loading Variation on Stator Airfoils.** Stator surface pressures were measured on two instrumented airfoils at locations described in Table 5 of Appendix A. For the large offset conditions of Compressor A, the instrumented vanes were moved to various circumferential positions from minimum to maximum rotor tip clearance to measure the respective stator loading.
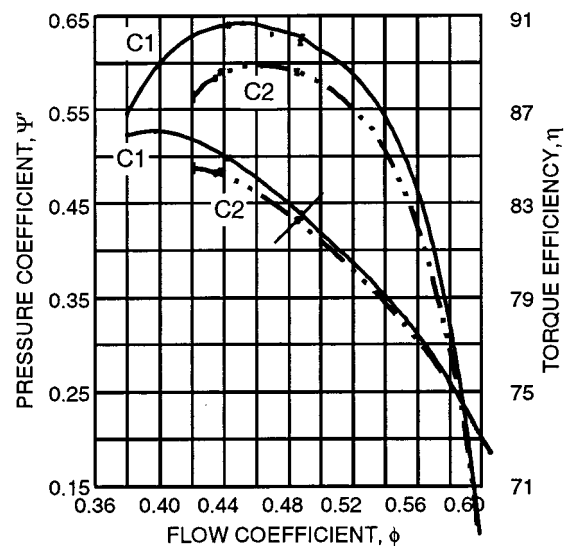
The resulting normalized, steady, surface static pressures as a function of percent airfoil chord are presented in Fig. 11(*a–i*). From left to right in the figure, we show the results for compressor low, medium, and high loading, respectively, taken at Test Points 1, 3 and 5 in Fig. 7. From top to bottom, we show the results from near the casing, at midspan and near the hub. In each of the nine parts of the figure, the circumferential variation in stator loading is presented for maximum, nominal, and minimum clearances.

One can identify the magnitudes of the stator incidence angle and leading edge loading in Fig. 11 by the amount of either cross-over or separation between the suction and pressure surface curves. For example, the crossover of these surface distributions at about 8 percent chord in Fig. 11(*d*) indicates lower incidence angle and lower leading edge loading compared to the large separation in these distributions near the leading edge for nominal clearance in Fig. 11(*c*).

Near the casing at 90 percent span, we see a progressive increase in the circumferential variation of stator incidence as one moves along the pressure characteristic from low compressor loading, Fig. 11(*a*), to medium loading, Fig. 11(*b*), to high loading, Fig. 11(*c*). Using data from the concentric tests, we computed an incidence angle derivative with respect to changes in leading edge loading. When this derivative was applied to the observed variation in the offset tests shown in Fig. 11, we found variations in incidence angle near the casing of up to 7 degrees around the circumference. Such a large circumferential variation in stator incidence angle and airfoil leading edge loading is clearly seen in Fig. 11(*c*).
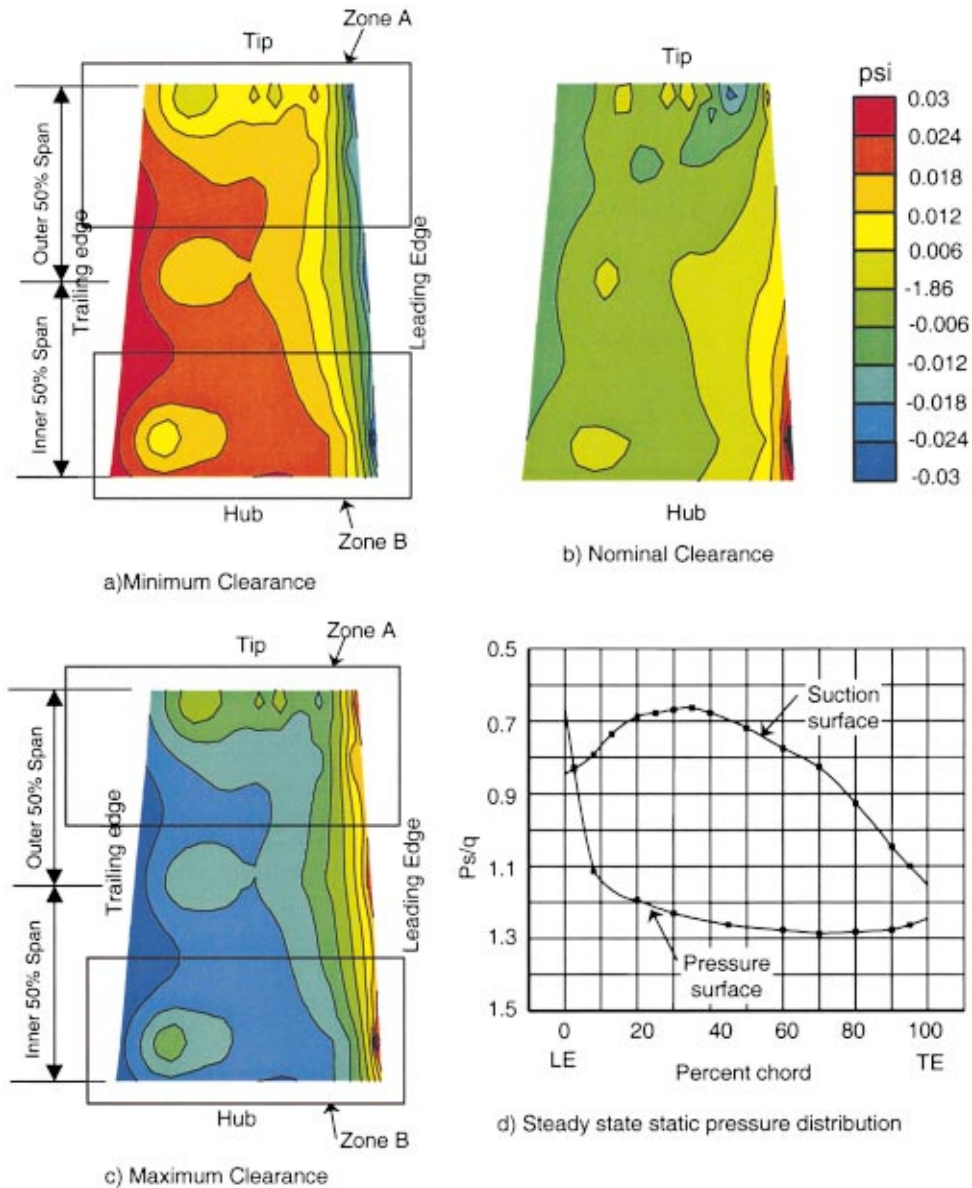
**Fig. 10** (*a, b, c*) **Contours of unsteady static pressure difference on the rotor airfoils at three clearance levels around the circumference for the large centerline offset. Zone *A* is affected by variation in rotor blade tip clearance and zone *B* is affected by stator shroud seal clearance. Both zones are affected by any radial flow redistribution; (*d*) chordwise distribution of measured, steady-state static pressure on rotor airfoil at 80 percent span.**

At midspan, there is no change in stator incidence around the circumference at low compressor loading, Fig. 11(*d*), with some increase in incidence variation as loading increases from Fig. 11(*e, f*). Near the hub, the influence of increased stator seal-tooth clearance makes itself known from Fig. 11(*g, h, i*).

The circumferential variations in stator loading seen near the hub in Fig. 11 imply circumferential variations in hub spool loading, which constitutes an additional driving mechanism for rotor whirl not previously incorporated into analyses. A discussion of this effect is given in Part II.

## 6.0 Unsteady Blade Forces and the Thomas/Alford Parameter $\beta$ Coefficient

In this section we present the unsteady blade forces that drive rotor whirl in compressors and the calculation of the Thomas/Alford parameter, or $\beta$ coefficient.

**6.1 Unsteady Whirl-Inducing Blade Forces.** The unsteady pressures presented in Section 5.1 were reduced to unsteady blade forces as described in Section 3.4. A representative result for the large offset configuration running at high compressor loading (Test Point 5 in Fig. 7) is shown in Fig. 12. The tangential and radial components of the unsteady, whirl-inducing blade force are plotted as a function of circumferential position. The circumferential variation of rotor tip clearance is also plotted.

The forces in Fig. 12 need to be understood relative to the sign convention of Fig. 13. The direction of rotation and the direction of the driving torque in Fig. 13 are counterclockwise. The centerline is offset upward, which places the minimum clearance at top-dead-center. Two forces are shown acting on each airfoil: a mean force, $F_m$, and the tangential component of the unsteady force due to the offset, $F_u$. The magnitude and direction of the unsteady force will determine the direction of rotor whirl.

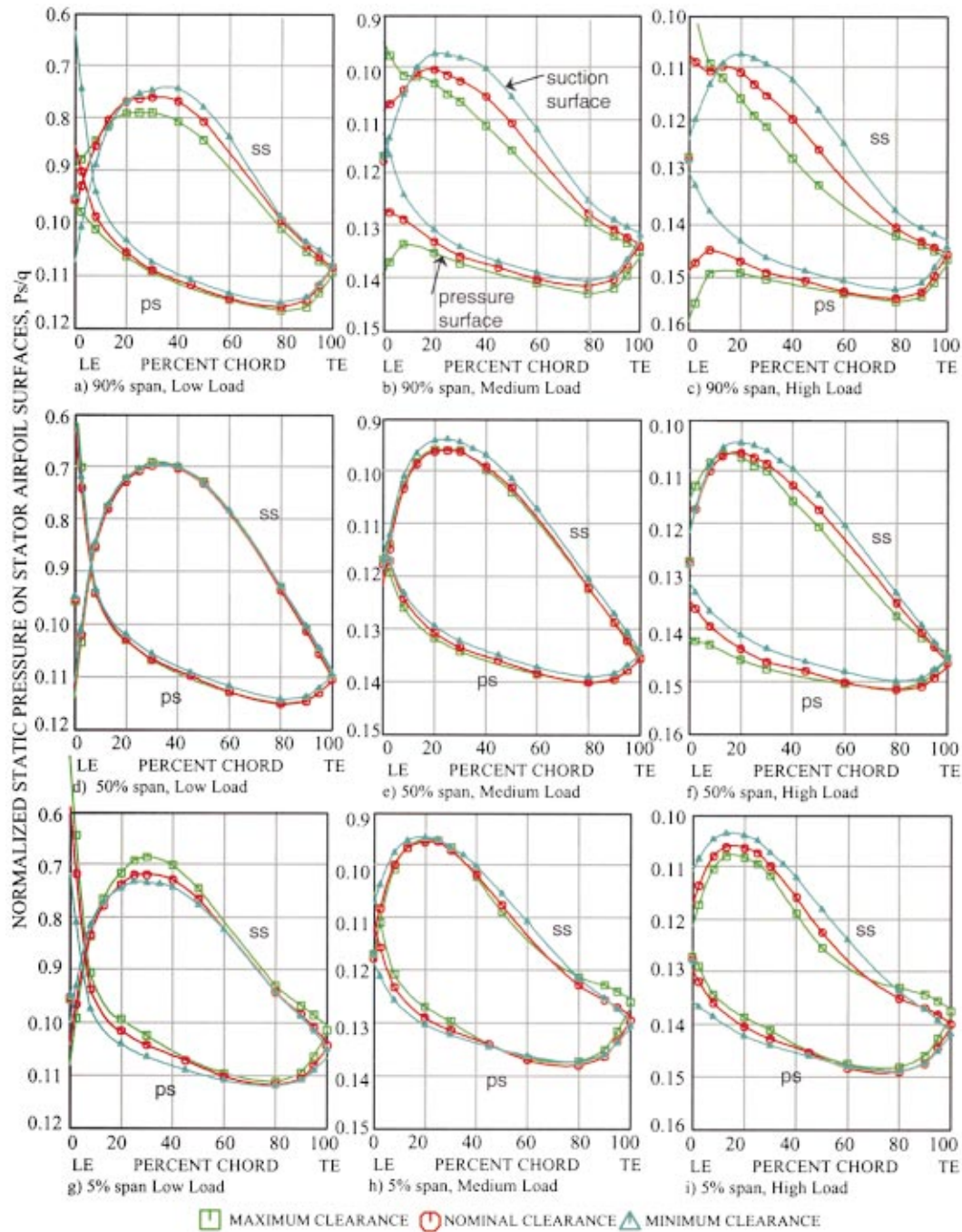In Fig. 12 the radial component of unsteady force is very small

**Fig. 11 Circumferential variation of stator airfoil loading for Compressor *A* showing the effects different levels of rotor tip clearance due to centerline offset. (*a–c*) 90 percent span; (*d–f*) 50 percent span; (*g–i*) 5 percent span. Low, medium, and high compressor loading were obtained at test points 1, 3, and 5, respectively, in Fig. 7.**

compared to the tangential component. The maximum tangential force occurs near the minimum clearance and the minimum tangential force occurs near the maximum clearance, again confirming the correctness of Ehrich's hypothesis. Careful use of the sign convention in Fig. 13 leads us to conclude that in the region of negative forces shown as Zone 1 in Fig. 12, the net forces acting on the airfoils increase because the unsteady force, $F_u$, adds vectorially to the mean force, $F_m$. This occurs around the minimum clearance. In the region of positive forces shown as Zone 2 in Fig. 12, the net forces on the airfoils decrease as the unsteady force, $F_u$, oppose the mean force, $F_m$. This occurs around maximum clearance near bottom dead center. The net effect of the force

distribution tends to drive the offset rotor shaft counter to the direction of rotation, i.e., it drives backward whirl.

The analysis of the data in Fig. 12 clearly shows that the whirl-inducing forces from centerline offset will tend to drive backward rotor whirl in compressors at this throttle setting.

The unsteady forces do not peak at the minimum clearance, but peak 40 deg from minimum tip clearance in the direction of rotation. This is due to fluid inertia effects as will be discussed in Part II of this paper.

**6.2 Stator Vane Tangential Force.** Stator surface pressures shown in Fig. 11 were integrated in the chordwise and span-
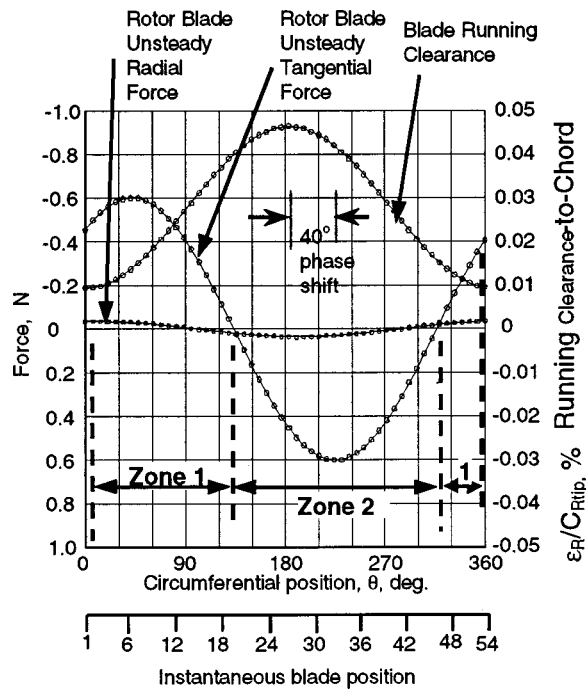
Fig. 12 Circumferential variation of the unsteady whirl inducing force components and running rotor tip clearance for the large centerline offset of LSRC Compressor A. Zone 1 is for net force increased and zone 2 for net force decreased. Data shown for Test Point 5 in Fig. 7; see Appendix B3a.
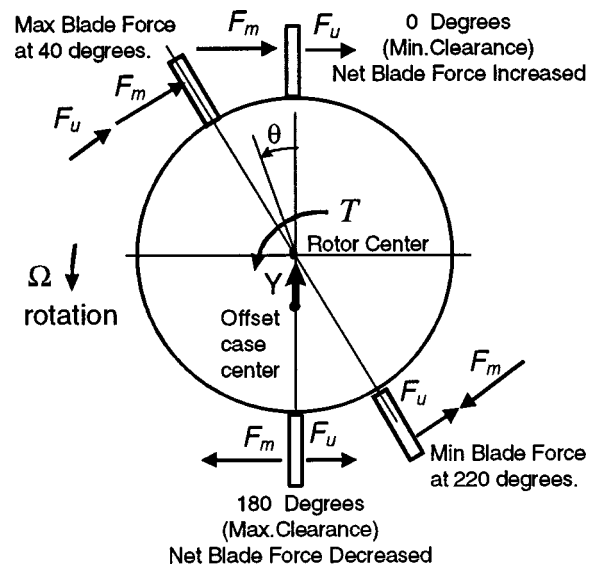


Fig. 13 Distribution of tangential blade force for LSRC Offset Rotor Test showing direction of mean and unsteady forces ($F_m$ and $F_u$) at various circumferential positions; see Appendices B1 and B3a
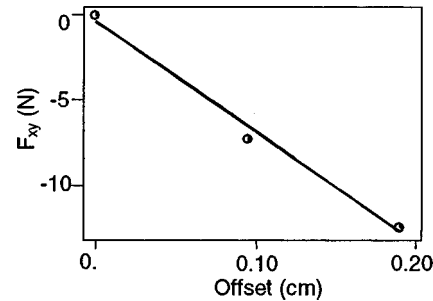


Fig. 14 Regression plot of cross-axis-force for high compressor loading test point 5 in Fig. 7

wise directions to obtain the aerodynamic forces. Tangential force component in the direction of rotor rotation was observed to vary around the circumference, in phase with the clearance variation. This force was largest in the region of minimum clearance and was smallest in the region of maximum clearance. This is similar to the force variation measured on the rotor blading.

**6.3 The $\beta$ Coefficient.** We computed the cross-axis and direct stiffness forces, $F_X$ and $F_Y$, for the two centerline offsets and the various values of compressor loading as discussed in Section 3.4. We then computed the cross-axis aerodynamic stiffness coefficient, $K_{XY}$. An example showing the cross-axis force versus offset is presented in Fig. 14 for Test Point 5 of Compressor A. The slope of this curve, $K_{XY}$, is linear to within a 0.225 variance. From that and the pertinent geometry and measured torque for the LSRC configuration, we computed the corresponding $\beta$ coefficient using Eq. (1). The stiffness forces and resulting $\beta$ coefficients are shown in Table 1. See Appendix B3c.

A curve-fit of the $\beta$ coefficients from Table 1 is shown in Fig.

15 for Compressor A. Clearly the Thomas/Alford force drives backward rotor whirl over most of the compressor operating range, although some regions of near-zero and positive whirl-inducing forces are observed at high flow coefficients greater than 0.44.

**7.0 Discussion**

The analysis of the data presented in Part I of this paper clearly shows that the Thomas/Alford forces in axial-flow compressors

Table 1 Stiffness forces and the $\beta$ coefficients for Compressor $A$: see Appendix B 3c

| Operating Condition | Test Pt. In Fig. 7 | 0.1905 cm offset (0.075 inches) | | 0.0965 cm offset (0.038 inches) | | Beta Coefficient |
|---|---|---|---|---|---|---|
| | | $F_X$ N/(lb) | $F_Y$ N/(lb) | $F_X$ N/(lb) | $F_Y$ N/(lb) | |
| Low Loading | 1 | 0.044 (0.01) | 2.27 (0.51) | -0.71 (-0.16) | 1.07 (0.24) | 0.24 |
| | 2 | -2.28 (-0.49) | 4.36 (0.98) | -1.16 (-0.26) | 2.63 (0.59) | -0.82 |
| Peak Efficiency | 3 | -4.49 (-1.01) | 5.87 (1.32) | -2.71 (-0.61) | 3.34 (0.75) | -1.64 |
| Design Point | 4 | -7.48 (-1.68) | 7.08 (1.59) | -4.13 (-0.93) | 4.36 (0.98) | -2.76 |
| | 5 | -12.41 (-2.79) | 9.65 (2.17) | -7.29 (-1.64) | 5.69 (1.28) | -4.63 |
| Peak Pressure - Near Stall | 6 | -16.51 (-3.71) | 17.53 (3.94) | -9.61 (-2.16) | 7.88 (1.77) | -6.58 |

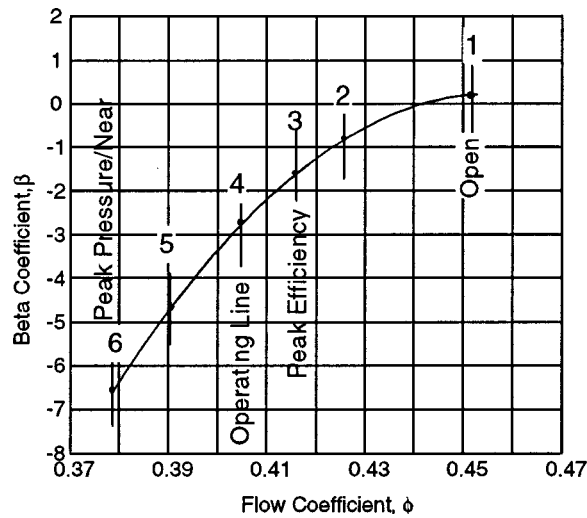**Fig. 15 Computed beta coefficients for the LSRC compressor *A* offset rotor test showing that unsteady forces promote backward whirl over most of the compressor operating range. Test Points 1−6 correspond to those in Fig. 7.**

typical of modern design tend to drive backward whirl. In fact, for off-design operation at lower flows and high airfoil loading, the beta coefficients were strongly negative.

However, there are qualifications that go along with our findings. Backward whirl-inducing forces do not occur over all of the operating points of the compressor map, as also clearly shown by our data. At high-flow, low-loading situations, the Thomas/Alford forces were neutral or shown to drive forward whirl, although the magnitudes of the positive $\beta$ coefficients were small.

In engine operation, the range of $\beta$ coefficients in Fig. 15 can be encountered during operating line migrations from the steady state design point. Low operating line (high flow coefficient) situations for the HP compressor occur for commercial engine operation primarily during a rapid deceleration from high power. An example of this could be a throttle chop *following* thrust reverser deployment on landing. In this situation fuel flow drops abruptly, causing the pressure in the combustor and rear of the compressor to drop. The operating line then drops but the rotational speed cannot change instantaneously so the pumping (air flow) is high.

High operating line (low flow coefficient) situations for the HP compressor occur primarily during a rapid engine spool-up (acceleration). This can occur during take-off, application of reverse thrust on landing, a go-around on missed approach, and aircraft avoidance maneuvers. Fuel flow to the combustor is increased raising its temperature and back-pressuring the compressor. This causes the operating line to go up before the rotational speed can increase appropriately.

## 8.0 Conclusions

The following conclusions about whirl-inducing aerodynamic forces in compressors can be drawn from the experimental data of Part I:

The long-standing disparity in findings concerning the direction and magnitude of rotor whirl-inducing, aerodynamic forces in axial-flow compression systems used in modern turbomachinery has been definitively resolved. The Thomas/Alford force drives backward rotor whirl over most of the compressor operating range. This means that the $\beta$ coefficients are mostly negative with some near-zero and small positive values (forward whirl) at high flow. Consequently, compressor whirl forces tend to promote whirl in the direction opposite to that of turbines over most of the operating range.

When the centerline of the rotor is displaced from the centerline of the casing, the *unsteady* loading on the rotor airfoils in the tighter clearance region increases and the *unsteady* loading on the rotor airfoils in the more-open clearance region decreases relative to the loading for nominal clearance.

The Ehrich model describing compressor whirl resulting from aerodynamic forces, as presented in Fig. 1(c), has been validated by the low-speed testing process. This important finding strongly suggests the model's correctness for use in guiding HP compressor designers.

The parallel compressor model has been validated for the offset tests, based on the analysis of the performance derivatives. This finding is important to the applicability of the analytical models in Part II.

The unsteady forces do not peak at the minimum clearance but peak 40 deg from minimum clearance in the direction of rotation for Compressor A. This is due to fluid inertia effects as will be discussed in Part II of this paper.

To date attention has been given only to the effects of rotor tip clearance. A new finding has shown that clearance variations in the hub region can also have a significant effect on the magnitude and direction of rotor whirl. This will be discussed in detail in Part II.

Large performance penalties in efficiency, pressure-rise capability and stall margin can occur if average and maximum clearances increase during rotor centerline displacement. Unsteady incidence angle variations around the circumference of as much as seven degrees were observed.

### Appendix A

**Tables 2−5 Giving Blading and Configuration Details**

**Table 2 Blading details for Compressors *A*, *B*, and *C* at midspan**

|  | IGV | | | ROTOR | | | STATOR | | |
|---|---|---|---|---|---|---|---|---|---|
|  | A | B | C | A | B | C | A | B | C |
| Solidity | 1.0 | 1.0 | 1.5 | 1.16 | 1.11 | 0.97 | 1.43 | 1.32 | 1.00 |
| Aspect Ratio | 1.36 | 1.36 | 1.5 | 1.20 | 1.25 | 1.83 | 1.34 | 1.45 | 2.05 |
| Chord, cm | 8.38 | 8.38 | 15.2 | 9.55 | 9.12 | 12.3 | 8.53 | 7.91 | 11.0 |
| Chord, inch | 3.3 | 3.3 | 6.0 | 3.76 | 3.59 | 4.86 | 3.36 | 3.114 | 4.33 |
| Stagger, deg. | 14.8 | 3.4 | 19.9 | 50.4 | 49.1 | 42.0 | 30.5 | 20.3 | 33.4 |
| Camber, deg. | -- | -- | -- | 31.8 | 32.3 | 32.4 | 40.5 | 53.4 | 40.4 |
| No. of Airfoils | 53 | 53 | 40 | 54 | 54 | 32 | 74 | 74 | 37 |

**Table 3  Values of clearances and offsets for Compressors *A*, *B*, and *C***

| | Rotor Tip Clearance | | | Stator Shroud-Seal Clearance | | | Centerline Offset | | |
|---|---|---|---|---|---|---|---|---|---|
| | $\epsilon_r$ cm | $\epsilon_r$ in | $\dfrac{\epsilon_r}{c_{rTIP}}$ % | $\epsilon_s$ cm | $\epsilon_s$ in | $\dfrac{\epsilon_s}{H}$ % | Y cm | Y in | $\dfrac{Y}{H}$,% |
| **Compressor A** | | | | | | | | | |
| A1. Baseline | 0.155 | 0.061 | 1.63 | 0.089 | 0.035 | 0.8 | 0 | 0 | 0 |
| A2. Nom R Open S | 0.155 | 0.061 | 1.63 | 0.178 | 0.070 | 1.6 | 0 | 0 | 0 |
| A3. Open R Nom S | 0.320 | 0.126 | 3.35 | 0.089 | 0.035 | 0.8 | 0 | 0 | 0 |
| A4. Open R Open S | 0.320 | 0.126 | 3.35 | 0.178 | 0.070 | 1.6 | 0 | 0 | 0 |
| A5. Small Offset | | | | | | | | | |
| Avg | 0.279 | 0.110 | 2.92 | 0.178 | 0.070 | 1.6 | 0.0965 | 0.038 | 0.711 |
| Min | 0.198 | 0.078 | 2.07 | 0.081 | 0.032 | 0.7 | 0.0965 | 0.038 | 0.711 |
| Max | 0.351 | 0.138 | 3.67 | 0.274 | 0.108 | 2.4 | 0.0965 | 0.038 | 0.711 |
| A6. Large Offset | | | | | | | | | |
| Avg | 0.251 | 0.099 | 2.63 | 0.284 | 0.112 | 2.5 | 0.191 | 0.075 | 1.67 |
| Min | 0.056 | 0.022 | 0.59 | 0.094 | 0.037 | 0.8 | 0.191 | 0.075 | 1.67 |
| Max | 0.437 | 0.172 | 4.57 | 0.475 | 0.187 | 4.2 | 0.191 | 0.075 | 1.67 |
| **Compressor B** | | | | | | | | | |
| B1. Baseline | 0.160 | 0.063 | 1.75 | 0.089 | 0.035 | 0.8 | 0 | 0 | 0 |
| B2. Nom R Open S | 0.160 | 0.063 | 1.75 | 0.178 | 0.070 | 1.6 | 0 | 0 | 0 |
| B3. Open R Nom S | 0.320 | 0.126 | 3.51 | 0.089 | 0.035 | 0.8 | 0 | 0 | 0 |
| **Compressor C** | | | | | | | | | |
| C1. Baseline(*) | 0.323 | 0.127 | 2.61 | 0.320 | 0.126 | 1.40 | 0 | 0 | 0 |
| C2.Open R Nom S(*) | 0.625 | 0.246 | 5.06 | 0.320 | 0.126 | 1.40 | 0 | 0 | 0 |

(*) cantilevered stator

**Table 4  Rotor blade kulite locations**

| Percent Chord on Suction Surface | | | | | | | | | | % Span | Percent Chord on Pressure Surface | | | | | | |
|---|---|---|---|---|---|---|---|---|---|---|---|---|---|---|---|---|---|
| 4 | 12 | 18 | 24 | 30 | 40 | 50 | 60 | 72 | 87 | 96.2 | | 12 | 18 | 24 | 30 | 50 | 80 |
| | 12 | 18 | | | 40 | | | | | 92.2 | | 12 | 18 | | 40 | | |
| | 11 | 18 | | 30 | | | | 72 | | 82.0 | | 11 | 18 | | 30 | | |
| 5 | 13 | | 21 | 30 | 40 | 55 | | 72 | 87 | 51.2 | 7.5 | 13 | | 21 | 30 | 50 | 80 |
| 5 | 12 | | | 30 | | | | 72 | | 20.5 | 6 | 12 | | | | | |
| 4 | 12 | | 21 | 30 | 40 | 50 | 60 | 72 | 87 | 10.2 | 5 | 12 | | 21 | 30 | 50 | 80 |

**Table 5  Stator vane pressure tap locations**

Five Rows – at the following percent immersion from casing:
10,  20,  50,  80,  and  95

| Tap Locations in Each Row | | | | | | | | | | | | | |
|---|---|---|---|---|---|---|---|---|---|---|---|---|---|
| Percent Chord on Stator Suction Surface | | | | | | | | | | | | | |
| 2.5 | 8 | 13 | 20 | 25 | 30 | 35 | 40 | 50 | 60 | 70 | 80 | 90 | 96 |
| Percent Chord on Stator Suction Surface | | | | | | | | | | | | | |
| 2.5 | 8 | | 20 | | 30 | 45 | 60 | 70 | | | 80 | 90 | 95 |

# Appendix B

## Sign Convention and Coordinate Systems

*B1  Direction of the Forces.*   Regarding $F_M$ and $F_U$ in Figs. 1 and 13, the arrows are drawn with the arrow head pointing in the direction that the forces act in the compressor and the turbine. For example in Fig. 2(*b*) at the top, the arrows show that the unsteady force $F_U$ will reduce the mean force $F_M$ as the arrows oppose each other. But at the top in Fig. 2(*c*), the arrows show that the unsteady force $F_U$ will increase the mean force $F_M$ as the arrows are in the same direction. $F_M$ and $F_U$ must be considered as a vector sum, as stated in the third paragraph of Section 6.1.

*B2  The Sign Convention.*   Following rotordynamic convention, we define forward and backward whirl relative to the direction of rotor rotation. This has a subtle aspect when looking at plus and minus directions in Cartesian coordinates. For engines rotating counterclockwise forward looking aft, positive whirl forces are those which will drive a whirling rotor counterclockwise. In Figs. 3 and 5, we show the force $F_X$ pointing from the origin to the LEFT as a positive force because it will drive the displaced centerline counterclockwise about the undisplaced centerline. To the casual observer, positive in Cartesian coordinates would be from the origin to the RIGHT.

*B3  The Coordinate Systems.*   Two coordinate systems are used, as described by Figs. 3 and 5. All of the forces are defined in the Nomenclature.

*a  The (local) coordinate system fixed to the blades.*   The tangential and radial forces that act on the rotor blades, $F_T$ and $F_R$, are shown schematically in Fig. 5 in a coordinate system fixed to the blades. The measured *unsteady* tangential and radial forces shown in Fig. 12 are in this coordinate system. Note that $F_T$ (rotor blade unsteady tangential force) in Fig. 12 is much larger than $F_R$ (rotor blade unsteady radial force). These unsteady forces, $F_T$ and $F_R$, are resolved into the total unsteady force, $F_U$, which is then added vectorially to the mean force, $F_M$, to get the total force on the airfoil as shown schematically in Fig. 13.

*b  The (global) coordinate system fixed to the rotor centerline*   The net unbalanced forces acting perpendicular and parallel to the shaft deflection, $F_X$ and $F_Y$ in Fig. 5, are in a coordinate system fixed to and acting about the rotor centerline as seen in Fig. 3. In this global system, $F_X$ is the cross-axis stiffness force that drives rotor whirl about the undisplaced centerline. $F_Y$ is the direct stiffness force.

The airfoils in the blade-fixed coordinate system rotate about this global coordinate system, with the angle of rotation, theta, shown in Figs. 5 and 13 as positive in the counterclockwise direction.

*c Transformation from local to global coordinate system*
Referring to Fig. 5, the transformation from the local to global coordinate system for the *i*th rotor blade is:

Global (rotor–disk)        Local blade-fixed
coordinate system          coordinate system

$$\begin{Bmatrix} F_X \\ F_Y \end{Bmatrix} = \begin{bmatrix} \cos(\theta) & \sin(\theta) \\ -\sin(\theta) & \cos(\theta) \end{bmatrix}_i \begin{Bmatrix} F_T \\ F_R \end{Bmatrix}_i$$

Summing the forces over all of the rotor blades is done as shown below.

$$F_X = \sum_{i=1}^{N_B} F_{Xi} \quad F_Y = \sum_{i=1}^{N_B} F_{Yi}$$

Note that the large unsteady tangential force, $F_T$, in Fig. 12 will contribute to *both* $F_X$ and $F_Y$ in Table 1 so that the values of $F_X$ and $F_Y$ can be of nearly the same magnitude. The key is that $F_X$ in Table 1 is *negative in sign*, which drives backward whirl over most of the operating range as shown by the negative beta coefficient.

## Nomenclature

$A$ = annulus area, m$^2$
$C_{\mathrm{Rtip}}$ = chord length at tip, cm
$D_p$ = mean blade diameter, m
$F_T, F_R, F_m$ = tangential, radial, and mean force on rotor blades, N
$F_X$ = net unbalanced force perpendicular to rotor deflection, N
$F_Y$ = net unbalanced force parallel to rotor deflection N
$F_U$ = unsteady blade force, N
$H$ = blade height cm
$K_{XY}$ = cross-coupled stiffness coefficient, N/m
$k = \Phi/\sqrt{\Psi'}$ = throttle coefficient
$\dot{m}$ = mass flow
$P_1, T_1$ = compressor inlet pressure and temperature, kPa, °C
$P_S$ = static pressure acting on blade surface, kPa
$q$ = $1/2\rho_{\mathrm{ref}}U_t^2$, dynamic pressure for normalizing pressures, kPa
$R_c$ = casing radius, cm
$R_H$ = hub radius cm
$R$ = radial coordinate
$T$ = stage torque, N-m
$T_{\mathrm{tan}}$ = blade tangential direction
$\mathrm{TM}$ = $[(k_D/k_S)-1] \times 100$, throttle margin, percent
$U$ = rotor wheel speed, m/s
$X$ = coordinate orthogonal to $Y$
$Y$ = vertical coordinate in direction of deflection
$+Y$ = rotor deflection, cm
$Z$ = axial coordinate
$\beta$ = normalized cross-coupled stiffness coefficient (the ''Thomas/Alford Coefficient'')

$\varepsilon_R$ = rotor tip clearance, cm
$\varepsilon_S$ = shroud seal clearance, cm
$\eta$ = $\Psi'/\Psi \times 100$ percent, torque efficiency, points
$\Phi = \dot{m}/\bar{\rho}A U_{,t}$ = flow coefficient
$\Psi = T/[(1/2)\bar{\rho}U_t^2\Phi R_t A]$ = work coefficient
$\Psi' = C_p T_1/(1/2)U_t^2[(\Delta P/p_1 + 1)^{(\gamma-1)/\gamma} - 1]$ = pressure coefficient
$\theta$ = blade azimuth angle, rad
$\rho$ = density
$\Omega$ = spin speed of the rotor, rad/s

### Superscripts

$-$ = averaged value

### Subscripts

$t$ = rotor tip
$D$ = design point
$s$ = stall point

## References

[1] Thomas, H. J., 1958, ''Unstable Natural Vibration of Turbine Rotors Induced by the Clearance Flow in Glands and Blading,'' Bull. de l'A.I.M., **71**, No. 11/12, pp. 1039–1063.
[2] Alford, J., 1965, ''Protecting Turbomachinery From Self-Excited Rotor Whirl,'' ASME J. Eng. Power, **8**, pp. 333–344.
[3] Kofskey, M. G., and Nusbaum, W. J., 1968, ''Performance Evaluation of a Two Stage Axial Flow Turbine for Two Values of Tip Clearance,'' NASA TN D4388.
[4] Urlichs, K., 1975, ''Clearance Flow-Generated Transverse Forces at the Rotors of Thermal Turbomachines,'' Dissertation, Technical University of Munich (English translation in NASA TM-77292, Oct. 1983).
[5] Urlichs, K., 1977, ''Leakage Flow in Thermal Turbo-Machines as the Origin of Vibration-Exciting Lateral Forces,'' NASA TT F-17409, Mar.
[6] Wohlrab, R., 1975, ''Experimental Determination of Gap Flow-Conditioned Force at Turbine Stages and Their Effect on Running Stability of Simple Rotors,'' Dissertation, Technical University of Munich (English translation in NASA TM-77293, Oct. 1983).
[7] Martinez-Sanchez, S., and Jaroux, B., 1991, ''Turbine Blade Tip and Seal Clearance Excitation Forces,'' M.I.T. Gas Turbine Laboratory, Cambridge, MA (Phase III Report on Contract No. NAS8-35018).
[8] Ehrich, F. F., 1993, ''Rotor Whirl Forces Induced by the Tip Clearance Effect in Axial Flow Compressors,'' ASME J. Vibr. Acoust., **115**, pp. 509–515.
[9] Vance, J. M., and Laudadio, F. J., 1994, ''Experimental Measurement of Alford's Force in Axial Flow Turbomachinery,'' ASME J. Eng. Gas Turbines Power, **106**, p. 585.
[10] Colding-Jorgensen, J., 1992, ''Prediction of Rotordynamic Destabilizing Forces in Axial Flow Compressor,'' ASME J. Fluids Eng., **114**, p. 621.
[11] Yan, L., Hong, J., Li, Q., Zhu, Z., and Zhao, Z., 1995, ''Blade Tip Destabilizing Force and Instability Analyses for Axial Rotors of Compressor,'' Beijing, University of Aeronautics and Astronautics, Beijing, China (AIAA Paper No. A95-40315).
[12] Akin, J. T., Fehr, V. S. and Evans, D. L., 1988, ''Analysis and Solution of the Rotor Instability Problem in the Advanced Model P111+ Engine,'' Paper No. AIAA-88-3166.
[13] Wisler, D. C., 1981, ''Compressor Exit Stage Study Volume IV—Data and Performance Report for the Best Stage,'' NASA CR-165357.
[14] Wisler, D. C., 1985, ''Loss Reduction in Axial-Flow Compressors Through Low-Speed Model Testing,'' ASME J. Eng. Gas Turbines Power, **107**, pp. 354–363.
[15] Wisler, D. C., Halstead, D. E., and Beacher, B. F. 1999, ''Improving Compressor and Turbine Performance Through Cost Effective Low-Speed Testing,'' ISABE99-7073, *Proc. 14th International Symposium on Air Breathing Engines*, Sept., Florence, Italy.
[16] Doebelin, E. O., 1975, *Measurement System*, McGraw-Hill, pp. 398–401.
[17] Wellborn, S., and Okiishi, T., 1999, ''Influence of Shrouded Stator Cavity Flows on Multistage Compressor Performance,'' ASME J. Turbomach., **121**, pp. 486–498.